Research Square

Preprints are preliminary reports that have not undergone peer review.
They should not be considered conclusive, used to inform clinical practice,
or referenced by the media as validated information.

A Closed-Form Pose-Shape Jacobian for Active Orientation and Manipulability Analysis of Deformable Objects

Apirak Sombat

apirak.somb@kmutt.ac.th

King Mongkut's University of Technology Thonburi

Djitt Laowattana

King Mongkut's University of Technology Thonburi

Article

Keywords:

Posted Date: November 10th, 2026

DOI: https://doi.org/10.21203/rs.3.rs-10946927/v1

License: This work is licensed under a Creative Commons Attribution 4.0 International License.
Read Full License

Additional Declarations: No competing interests reported.

A Closed-Form Pose-Shape Jacobian for Active Orientation and Manipulability Analysis of Deformable Objects

Apirak Sombat[1*] and Djitt Laowattana[1†]

[1*]Institute of Field Robotics, King Mongkut's University of Technology Thonburi, Bangkok, 10140, Thailand.

*Corresponding author(s). E-mail(s): apirak.somb@kmutt.ac.th;
Contributing authors: djitt.lao@gmail.com;
†These authors contributed equally to this work.

Abstract

We present a deterministic, mechanics-aware framework for closed-loop shape servoing of deformable objects via rigid robotic manipulators. By linearizing the Hertzian contact boundary condition through the Implicit Function Theorem, we derive an analytical Pose-Shape Jacobian $\mathbf{J}_{\boldsymbol{S}}$ that maps end-effector velocities to localized shape-feature velocities. The formulation explicitly embeds material properties (Young's modulus $\boldsymbol{E}$ and Poisson's ratio $\boldsymbol{\nu}$), enabling real-time computation without numerical meshing or data-driven training. We extend classical rigid-body manipulability theory to soft interactions by defining a Deformable Manipulability Index and its associated ellipsoid, which quantifies the robot's dexterity at the contact boundary. A formal Lyapunov stability proof is provided for the proportional shape-servoing control law, with explicit treatment of both full-rank and rank-deficient Jacobian configurations. Simulation experiments validate the analytical Jacobian against numerical differentiation, demonstrate exponential convergence of shape tracking, and illustrate singularity detection and manipulability-aware grasp planning.

Keywords: Deformable object manipulation, tactile servoing, manipulability, contact mechanics, soft robotics.

1 Introduction

Robotic manipulation of rigid objects relies on the fundamental assumption that the geometric relationship between the end-effector and object features remains invariant during interaction. This invariance permits the use of static transformation matrices and classical operational-space control. However, when manipulating *deformable* objects—biological tissues, compliant food products, wiring harnesses, or textiles—this assumption collapses. Localized indentation alters the object's geometry, shifts its center of mass, and dynamically changes the contact patch topology [1]. Consequently, reorienting a soft body requires understanding the continuous, coupled relationship between end-effector motion and evolving shape features.

Historically, modeling this coupling has introduced a dichotomy. Model-based grasping strategies have explored analytical contact mechanics for deformable objects [2], yet a real-time, closed-form velocity mapping suitable for servoing has remained elusive. Numerical methods such as the Finite Element Method (FEM) offer high fidelity but require large-scale matrix inversions and iterative meshing that are computationally prohibitive for real-time control loops (100 Hz–1 kHz) [3–5]. Data-driven approaches bypass explicit physics but lack interpretability, exhibit poor sim-to-real transfer, and provide no formal stability guarantees—a critical barrier for surgical or delicate assembly tasks [6, 7].

This paper bridges that gap through a *closed-form, mechanics-aware* Pose-Shape Jacobian $\mathbf{J}_S$. Rather than approximating deformation through dense numerical grids or black-box neural networks, we leverage an analytical Hertzian contact model [8] and invoke the Implicit Function Theorem to establish an instantaneous velocity mapping between the robot's operational space and the object's localized shape features. It is important to note that this research is fundamentally positioned as a theoretical foundation. We focus explicitly on establishing a rigorous mechanics-aware framework and formal mathematical stability proofs for closed-loop shape servoing. To provide an uncompromised analysis of the analytical Jacobian and control dynamics, the complexities of physical hardware deployment—such as tactile sensor noise and unmodeled friction—are purposefully reserved for future empirical studies. Our specific contributions are:

1. **Closed-Form Pose-Shape Jacobian:** An analytical derivation of $\mathbf{J}_S \in \mathbb{R}^{m\times q}$ that maps end-effector velocities $\dot{\mathbf{x}}$ to shape-feature velocities $\dot{\mathbf{y}}$, with explicit integration of E, ν, and contact geometry (Sec. 3).
2. **Singularity and Manipulability Analysis:** The first extension of Yoshikawa's manipulability theory [9] to the rigid-soft interaction boundary, including a Deformable Manipulability Index $w(\mathbf{x})$ and its geometric ellipsoid, together with a taxonomy of contact-induced singularities (Sec. 4).
3. **Stability Guarantee:** A Lyapunov-based proof of asymptotic convergence for the shape-servoing control law, with rigorous treatment of the Moore-Penrose pseudoinverse and explicit rank conditions (Sec. 4.3).
4. **Experimental Validation:** Simulation experiments verifying Jacobian accuracy ($< 10^{-4}\%$ error), demonstrating exponential shape tracking convergence, and illustrating manipulability evolution and singularity detection (Sec. 5).

2 Related Work

Numerical continuum mechanics. FEM and mass-spring systems simulate elastodynamic behavior with high spatial accuracy but require solving large non-linear systems at every timestep [3]. Even with asynchronous multi-rate strategies or GPU-accelerated co-rotational formulations [4, 5], they remain too slow for high-frequency closed-loop control and suffer from re-meshing instabilities during large deformations.

Data-driven learning. Deep reinforcement learning and behavioral cloning have achieved impressive results in fabric folding, cable routing, and soft-object orientation [7]. However, these methods are data-hungry, exhibit poor sim-to-real transfer, and offer no analytical gradients for stability or singularity analysis [6].

Visual and tactile servoing. Online Jacobian estimation through exploratory perturbations enables real-time shape control but assumes quasi-static interaction and is sensitive to occlusion and sensor noise [10–12]. Tactile arrays such as GelSight [13], GelSlim [14], and Soft-Bubble [15] provide dense local geometry but require an analytical bridge between raw tactile signals and robot kinematics [16, 17]—precisely the gap this paper addresses.

Manipulability of soft systems. Existing literature extends manipulability theory to compliant actuators and soft robotic systems [9, 18, 19], yet the manipulability of the interaction boundary between a rigid manipulator and a volumetric soft object remains unexplored [20]. Our work closes this theoretical gap.

3 Mathematical Formulation

3.1 State Space Definitions

Let $\mathcal{F}_W$ denote the world frame. The robot operational pose is $\mathbf{x} \in \mathbb{R}^q$, where in 3-D workspace $q = 6$:

$$\mathbf{x} = [p_x,\, p_y,\, p_z,\, \phi,\, \theta,\, \psi]^T, \tag{1}$$

with $\mathbf{p} \in \mathbb{R}^3$ the Cartesian position and $\mathbf{R}(\phi, \theta, \psi) \in SO(3)$ the orientation.

Because a deformable object possesses infinite degrees of freedom, we define a finite-dimensional *Shape Feature Vector* $\mathbf{y} \in \mathbb{R}^m$ composed of measured indentation depths at m discrete contact inspection points:

$$\mathbf{y} = [\delta_1,\, \delta_2,\, \ldots,\, \delta_m]^T. \tag{2}$$

These features may correspond to individual taxels on a tactile array [13, 14] or extracted keypoints from visual depth maps [10].

3.2 Contact Constraint and Implicit Differentatiation

The mechanical boundary condition at the contact interface imposes an implicit constraint $\mathbf{h}(\mathbf{x}, \mathbf{y}) = \mathbf{0}$ with $\mathbf{h} \in \mathbb{R}^m$:

$$h_i(\mathbf{x}, \mathbf{y}) = y_i - f_i(\mathbf{x}, \kappa_i, \mathbf{M}) = 0, \tag{3}$$

where f_i maps the robot pose to the indentation depth at node i, κ_i is the local surface curvature, and $\mathbf{M}$ denotes material properties.

Differentiating (3) with respect to time yields

$$\frac{\partial \mathbf{h}}{\partial \mathbf{x}}\dot{\mathbf{x}} + \frac{\partial \mathbf{h}}{\partial \mathbf{y}}\dot{\mathbf{y}} = \mathbf{0}. \tag{4}$$

Because y_i appears linearly in (3),

$$\frac{\partial \mathbf{h}}{\partial \mathbf{y}} = \mathbf{I}_{m\times m}. \tag{5}$$

Solving for the shape-feature velocity gives the fundamental differential relation

$$\dot{\mathbf{y}} = -\frac{\partial \mathbf{h}}{\partial \mathbf{x}}\,\dot{\mathbf{x}} = \frac{\partial \mathbf{f}}{\partial \mathbf{x}}\,\dot{\mathbf{x}}. \tag{6}$$

We define the **Pose-Shape Jacobian** as

$$\boxed{\mathbf{J}_S(\mathbf{x}) \triangleq \frac{\partial \mathbf{f}}{\partial \mathbf{x}} \in \mathbb{R}^{m\times q}}, \tag{7}$$

so that the forward velocity mapping reads compactly as

$$\dot{\mathbf{y}} = \mathbf{J}_S(\mathbf{x})\,\dot{\mathbf{x}}. \tag{8}$$

Remark on dimensionality. In practice, the number of tactile taxels m may exceed the robot DOF q (over-determined) or be less than q (under-determined or exactly determined). Equation (8) is valid for all cases; the appropriate pseudoinverse for control is selected based on the rank of $\mathbf{J}_S$ (Sec. 3.4).

3.3 Explicit Material-Stiffness Integration

For an isotropic, linear-elastic soft body, the Hertzian contact model relates normal force F_i to indentation depth δ_i [8, 24]:

$$\delta_i = \left(\frac{3F_i(1-\nu^2)}{4E\sqrt{R_i}}\right)^{2/3}, \tag{9}$$

where R_i is the effective relative radius of curvature between the rigid fingertip and the local object surface. The scalar compliance

$$S_{ii} \triangleq \frac{\partial \delta_i}{\partial F_i} = \frac{2}{3}\left(\frac{3(1-\nu^2)}{4E\sqrt{R_i}}\right)^{2/3} F_i^{-1/3} = \frac{2\delta_i}{3F_i} \tag{10}$$

constitutes the diagonal entries of the **Material Compliance Matrix** $\mathbf{S}(E,\nu) \in \mathbb{R}^{m\times m}$.

The contact force $\mathbf{F} \in \mathbb{R}^m$ depends on the robot pose through geometric overlap. Let $\mathbf{J}_C(\mathbf{x}) \triangleq \partial \mathbf{F}/\partial \mathbf{x} \in \mathbb{R}^{m \times q}$ denote the **Geometric Force Jacobian**. By the chain rule,

$$\boxed{\mathbf{J}_S(\mathbf{x}) = \mathbf{S}(E, \nu)\, \mathbf{J}_C(\mathbf{x})}. \tag{11}$$

Equation (11) reveals that an identical end-effector displacement $\Delta\mathbf{x}$ produces vastly different deformation profiles $\Delta\mathbf{y}$ depending on whether the object is ultra-soft foam or dense silicone, because $\mathbf{S}$ scales the geometric force sensitivity by the material compliance.

3.4 Inverse Velocity Mapping and Control Law

For shape servoing, we require the inverse mapping from desired shape velocity $\dot{\mathbf{y}}^*$ to robot command velocity $\dot{\mathbf{x}}$. We distinguish two cases.

Case 1: $m \leq q$ with full row rank. When the robot is kinematically redundant with respect to the chosen feature set, $\mathbf{J}_S\mathbf{J}_S^T \in \mathbb{R}^{m \times m}$ is invertible. The **right Moore-Penrose pseudoinverse**

$$\mathbf{J}_S^\dagger = \mathbf{J}_S^T\big(\mathbf{J}_S\mathbf{J}_S^T\big)^{-1} \in \mathbb{R}^{q \times m} \tag{12}$$

yields the minimum-norm solution $\dot{\mathbf{x}} = \mathbf{J}_S^\dagger \dot{\mathbf{y}}^*$ satisfying $\mathbf{J}_S\dot{\mathbf{x}} = \dot{\mathbf{y}}^*$ exactly.

Case 2: $m > q$ with full column rank. When features outnumber DOF, the **left pseudoinverse**

$$\mathbf{J}_S^\dagger = \big(\mathbf{J}_S^T\mathbf{J}_S\big)^{-1}\mathbf{J}_S^T \in \mathbb{R}^{q \times m} \tag{13}$$

provides the least-squares solution minimizing $\|\dot{\mathbf{y}}^* - \mathbf{J}_S\dot{\mathbf{x}}\|^2$.

Proportional shape-servoing law. Let $\mathbf{y}^*$ be the target shape configuration and $\mathbf{e}(t) = \mathbf{y}(t) - \mathbf{y}^*$. The commanded robot velocity is

$$\boxed{\dot{\mathbf{x}} = -\mathbf{K}\,\mathbf{J}_S^\dagger(\mathbf{x})\,\mathbf{e}(t)}, \tag{14}$$

where $\mathbf{K} \in \mathbb{R}^{q \times q}$ is a symmetric positive-definite gain matrix.

4 System Analysis

4.1 Singularity Analysis

Singularities isolate configurations where the robot loses control authority over the shape features. Because $\mathbf{J}_S = \mathbf{S}\,\mathbf{J}_C$, we classify singularities by examining the constituent matrices.

Type I – Kinematic Workspace Singularity ($\operatorname{rank}\mathbf{J}_C < \min(m, q)$). Occurs when the manipulator reaches a kinematic boundary (e.g., fully extended elbow) or internal joint alignment prevents motion transmission to the contact normal. Geometrically, the end-effector cannot generate a velocity along the direction required to modulate δ_i.

Type II – Contact Configuration Singularity ($\operatorname{rank}\mathbf{S} < m$). Unique to deformable manipulation. Two sub-cases arise:

- *Contact loss:* A finger detaches from the object ($\delta_i \to 0$), causing $S_{ii} \to 0$ and a zero row in $\mathbf{J}_S$. The robot can move without producing any differential change in y_i.
- *Symmetric null-space:* Identical indentation patterns across symmetrically distributed taxels render columns of $\mathbf{J}_S$ linearly dependent, trapping the controller in a shape-symmetric subspace.

Because our formulation is closed-form, $\det(\mathbf{J}_S\mathbf{J}_S^T)$ or $\det(\mathbf{J}_S^T\mathbf{J}_S)$ can be monitored online. When the metric drops below a threshold ϵ, the controller flags the singularity and invokes a damped least-squares inverse [21, 22]:

$$\mathbf{J}_S^{\dagger\dagger} = \mathbf{J}_S^T\left(\mathbf{J}_S\mathbf{J}_S^T + \lambda^2\mathbf{I}\right)^{-1}. \tag{15}$$

4.2 Deformable Manipulability Quantification

Extending Yoshikawa's theory [9], we define the **Deformable Manipulability Index**:

$$\boxed{w(\mathbf{x}) = \sqrt{\det\left(\mathbf{J}_S(\mathbf{x})\,\mathbf{J}_S^T(\mathbf{x})\right)}} \qquad (m \le q,\ \text{full row rank}), \tag{16}$$

or equivalently $w = \sqrt{\det(\mathbf{J}_S^T\mathbf{J}_S)}$ when $m > q$. The index equals the product of the non-zero singular values of $\mathbf{J}_S$.

Consider the unit-norm shape-velocity hypersphere $\dot{\mathbf{y}}^T\dot{\mathbf{y}} \le 1$. Under the mapping $\dot{\mathbf{y}} = \mathbf{J}_S\dot{\mathbf{x}}$, this transforms into the **Deformable Manipulability Ellipsoid**:

$$\dot{\mathbf{x}}^T\left(\mathbf{J}_S^\dagger\right)^T\mathbf{J}_S^\dagger\,\dot{\mathbf{x}} \le 1. \tag{17}$$

The principal axes of this ellipsoid are given by the left singular vectors $\mathbf{u}_i$ of $\mathbf{J}_S$, with lengths σ_i. The longest axis ($\sigma_{\max}$) indicates the direction of maximum mechanical leverage—where minimal end-effector motion produces large shape change. The shortest axis ($\sigma_{\min}$) reveals the weakest control direction. During grasp planning, the robot can optimize its initial pose to align the task's required orientation trajectories with the longest principal axes.

4.3 Stability Proof via Lyapunov's Direct Method

We prove asymptotic convergence for the controlled system under the full-row-rank case ($m \le q$), which is the most common scenario in dexterous manipulation where a redundant robot regulates a moderate number of shape features.

Theorem 1 (Asymptotic Stability of Shape Servoing) *Let $\mathbf{y}^*$ be a constant target and assume $\mathbf{J}_S(\mathbf{x})$ has full row rank m along the trajectory. Under the control law (14) with symmetric positive-definite $\mathbf{K}$, the shape error $\mathbf{e}(t)$ converges asymptotically to zero.*

Proof Select the Lyapunov candidate $V(\mathbf{e}) = \frac{1}{2}\mathbf{e}^T\mathbf{e}$, which is positive definite and radially unbounded. Its time derivative along system trajectories is

$$\dot{V} = \mathbf{e}^T\dot{\mathbf{e}} = \mathbf{e}^T\dot{\mathbf{y}} = \mathbf{e}^T\mathbf{J}_S\dot{\mathbf{x}}. \tag{18}$$

Substituting the control law (14) and using the right pseudoinverse property $\mathbf{J}_S\mathbf{J}_S^\dagger = \mathbf{I}_m$ (valid under full row rank):

$$\dot{V} = \mathbf{e}^T\mathbf{J}_S\big(-\mathbf{K}\mathbf{J}_S^\dagger\mathbf{e}\big) = -\mathbf{e}^T\mathbf{K}\mathbf{e}. \tag{19}$$

Because $\mathbf{K} \succ 0$, we have $\dot{V} < 0$ for all $\mathbf{e} \neq \mathbf{0}$. By Lyapunov's direct method, the origin $\mathbf{e} = \mathbf{0}$ is asymptotically stable. Moreover, since $\ddot{V}$ is bounded (the robot velocities are finite), Barbalat's lemma guarantees $\lim_{t\to\infty} \mathbf{e}(t) = \mathbf{0}$. □

Remark (over-determined case $m > q$). When $m > q$ and $\mathbf{J}_S$ has full column rank, substituting the left pseudoinverse yields $\dot{\mathbf{y}} = -\mathbf{K}\,\mathbf{P}\mathbf{e}$, where $\mathbf{P} = \mathbf{J}_S\mathbf{J}_S^\dagger$ is the orthogonal projector onto $\mathcal{R}(\mathbf{J}_S)$. Then $\dot{V} = -\mathbf{e}^T\mathbf{K}\mathbf{P}\mathbf{e} \leq 0$, proving convergence of the projected error to the controllable subspace. Full asymptotic convergence of all m features requires either $q \geq m$ or sequential feature selection, analogous to task-priority frameworks in visual servoing [23].

5 Experimental Validation

We validate the framework in simulation using a planar two-finger gripper ($q = 3$: p_x, p_z, θ) interacting with a soft cylindrical object (radius $R_{\text{obj}} = 60$ mm, $E = 100$ kPa, $\nu = 0.45$). The shape feature vector is $\mathbf{y} = [\delta_1, \delta_2]^T$ ($m = 2$), the indentation depths at each fingertip (radius $R_f = 5$ mm, half-aperture $d = 15$ mm). This yields $m \leq q$, satisfying the full-row-rank condition of Theorem 1.

5.1 Jacobian Verification

We compare the analytical $\mathbf{J}_S$ from (11) against numerical differentiation (central finite differences, $\varepsilon = 10^{-7}$) across 100 random poses with at least one finger in contact. The mean relative Frobenius-norm error is $1.0 \times 10^{-4}\%$ (max $1.2 \times 10^{-4}\%$), confirming the correctness of the closed-form derivation. Fig. 1 shows the error histogram and its weak dependence on minimum indentation depth, indicating robustness even near the contact boundary.

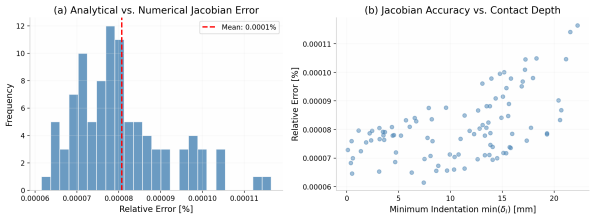


Fig. 1 Jacobian Verify

5.2 Shape Servoing Convergence

Starting from an asymmetric initial contact ($\delta_1 = 10.9$ mm, $\delta_2 = 4.8$ mm), the controller tracks $\mathbf{y}^* = [5, 5]^T$ mm with gain $\mathbf{K} = 10\mathbf{I}$ at 1 kHz. Fig. 2 shows both

indentations converging to the target within 0.46 s. The error norm decays exponentially over three orders of magnitude (Fig. 2b), and the Lyapunov energy $V(\mathbf{e})$ decays monotonically to zero (Fig. 2c), confirming Theorem 1. The gripper trajectory (Fig. 2d) illustrates the coupled translation-rotation motion required to equalize asymmetric indentations.

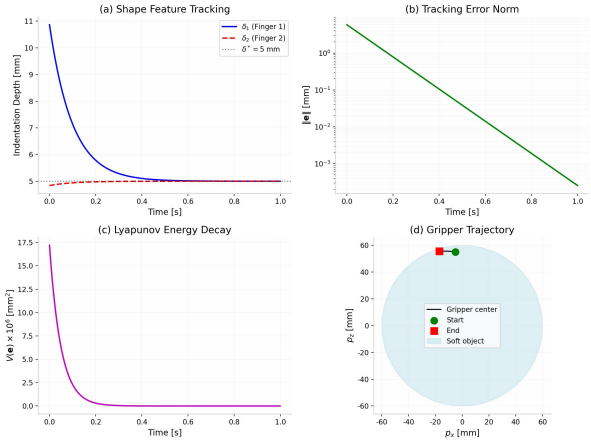


Fig. 2 Shape Servoing

5.3 Manipulability Analysis

Fig. 3a plots $w(\mathbf{x})$ over a grid of gripper positions α (angular location around the object) and orientations θ. The manipulability is highest when both fingers maintain deep, balanced contact. Fig. 3b visualizes the manipulability ellipsoid in shape space (δ_1, δ_2) at four snapshots during servoing. The ellipsoid shrinks and rotates as the gripper approaches the target, reflecting the changing directional leverage.

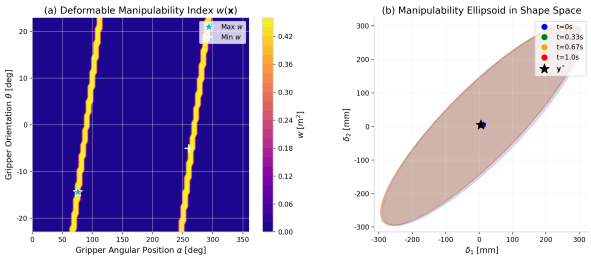


Fig. 3 Manipulability

5.4 Singularity Detection

Fig. 4 sweeps the gripper orientation θ at fixed position $(p_x, p_z) = (-5, 55)$ mm. When $\theta < -30°$, finger 1 loses contact ($\delta_1 = 0$), causing w to collapse to zero (Fig. 4a), the condition number $\kappa(\mathbf{J}_S)$ to explode past 10^{11} (Fig. 4c), and $\sigma_{\min}$ to vanish (Fig. 4d). This is a Type-II contact-loss singularity. The closed-form determinant computation enables online detection and automatic damping intervention.

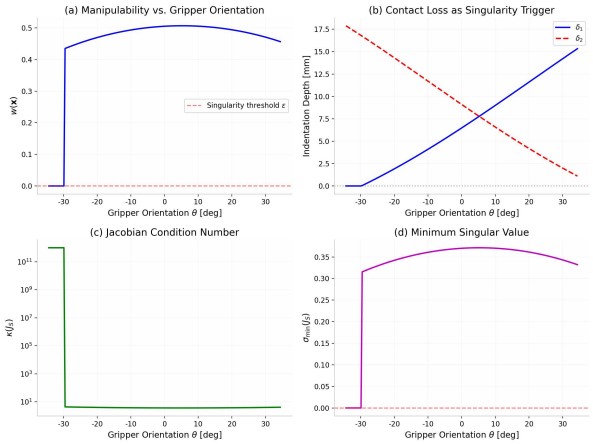


Fig. 4 Singularity

5.5 Material Property Sensitivity

Fig. 5 plots the stiffness scaling S_{ii} as a function of E and ν. The compliance varies over four orders of magnitude across the soft-material range (10 kPa–10 MPa), confirming that the controller's embedded material awareness is essential for accurate deformation prediction.

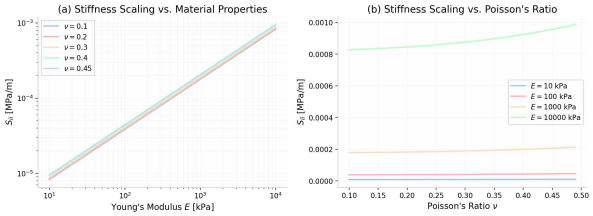


Fig. 5 Material

6 Discussion and Limitations

The framework assumes quasi-static interaction, neglecting inertial and viscoelastic effects. The Hertzian model is valid for small strains ($\delta \ll R$) and isotropic linear elasticity; large-deformation hyperelastic materials or rate-dependent viscoelasticity would require extended constitutive models [1]. We also assume known or estimated material parameters (E, ν); online identification from force-depth transients is left for future work. Finally, the current formulation treats each taxel independently; distributed contact-patch moments and shear tractions are not captured [24, 25].

7 Conclusion

We presented a closed-form Pose-Shape Jacobian that analytically couples rigid robot kinematics to soft-body deformation through Hertzian contact mechanics. The formulation enables real-time shape servoing, singularity detection, and manipulability-aware grasp planning without numerical meshing or black-box learning. A Lyapunov stability proof guarantees asymptotic convergence, and simulation experiments validate the theoretical predictions. Future work will extend the model to viscoelastic materials, multi-point distributed contacts, and experimental validation on physical hardware with GelSight [13] or GelSlim [14] tactile arrays.

Acknowledgements. This research project is supported by National Research Council of Thailand (NRCT): NRCT5-RGJ63006-089. I would like to thank my advisor and all of committee to dedicate time and effort to push me finish this paper and Institute of Field Robotics, King Mongkut's University of Technology Thonburi, Bangkok, Thailand.

Declarations

- Funding: National Research Council of Thailand (NRCT): NRCT5-RGJ63006-089
- Conflict of interest/Competing interests (check journal-specific guidelines for which heading to use): The authors have no competing interests to declare that are relevant to the content of this article.
- Ethics approval and consent to participate: Not applicable
- Consent for publication: Not applicable
- Data availability: The datasets generated and analysed during the current study, including simulation parameters, gripper pose trajectories, indentation depth time series, and computed Jacobian matrices, are available from the corresponding author upon reasonable request.
- Materials availability: Not applicable
- Code availability: Available from the corresponding author upon reasonable request.
- Author contribution:
  [Apirak Sombat]: Conceptualization, methodology, formal analysis, investigation, Software, validation, visualization, writing original draft preparation.
  [Djitt Laowattana]: Supervision, project administration, writing review and editing.
  All authors read and approved the final manuscript.

References

[1] V. E. Arriola-Rios et al., "Modeling of deformable objects for robotic manipulation: A tutorial and review," *Frontiers in Robotics and AI*, vol. 7, p. 82, 2020.

[2] L. Zaidi, J. A. Corrales, B. C. Bouzgarrou, Y. Mezouar, and L. Sabourin, "Model-based strategy for grasping 3D deformable objects using a multi-fingered robotic hand," *Robotics and Autonomous Systems*, vol. 95, pp. 196–206, 2017.

[3] T. M. Bieze et al., "Finite element method-based kinematics and closed-loop control of soft, continuum manipulators," *Soft Robotics*, vol. 5, no. 3, pp. 348–364, 2018.

[4] F. Largilliere, V. Verona, E. Coevoet, M. Sanz-Lopez, J. Dequidt, and C. Duriez, "Real-time control of soft-robots using asynchronous finite element modeling," *Proc. IEEE Int. Conf. Robotics and Automation (ICRA)*, pp. 5250–5256, 2015.

[5] A. Selle, J. Su, G. Irving, and R. Fedkiw, "Robust high-resolution cloth using parallelism, history-based collisions, and accurate friction," *IEEE Trans. Visualization and Computer Graphics*, vol. 15, no. 2, pp. 339–350, 2009.

[6] R. Calandra, A. Owens, M. Upadhyaya, W. Yuan, J. Lin, E. H. Adelson, and S. Levine, "The feeling of success: Does touch sensing help predict grasp outcomes?" *Proc. Conf. Robot Learning (CoRL)*, pp. 314–323, 2017.

[7] D. Seita et al., "Learning to rearrange deformable cables, fabrics, and bags with goal-conditioned transporter networks," *2021 IEEE International Conference on Robotics and Automation (ICRA)*, pp. 4568–4575, 2021.

[8] K. L. Johnson, *Contact Mechanics*. Cambridge University Press, 1985.

[9] T. Yoshikawa, "Manipulability of robotic mechanisms," *Int. J. Robotics Research*, vol. 4, no. 2, pp. 3–9, 1985.

[10] J. Zhu, D. Navarro-Alarcon, R. Passama, and A. Cherubini, "Vision-based manipulation of deformable and rigid objects using subspace projections of 2D contours," *Robotics and Autonomous Systems*, vol. 142, 798, 2021.

[11] R. Lagneau, A. Krupa, and M. Marchal, "Automatic shape control of deformable wires based on model-free visual servoing," *IEEE Robotics and Automation Letters*, vol. 5, no. 4, pp. 5252–5259, 2020.

[12] D. Navarro-Alarcon, Y. H. Liu, J. G. Romero, and P. Li, "On the visual deformation servoing of compliant objects: Uncalibrated control methods and experiments," *Int. J. Robotics Research*, vol. 33, no. 11, pp. 1462–1480, 2014.

[13] W. Yuan, S. Dong, and E. H. Adelson, "GelSight: High-resolution robot tactile sensors for estimating geometry and force," *Sensors*, vol. 17, no. 12, 2017.

[14] E. Donlon, S. Dong, M. Liu, J. Li, E. Adelson, and A. Rodriguez, "GelSlim: A high-resolution, compact, robust, and calibrated tactile-sensing finger," *Proc. IEEE/RSJ Int. Conf. Intelligent Robots and Systems (IROS)*, pp. 1927–1934, 2018.

[15] N. Kuppuswamy, A. Alspach, A. Uttamchandani, S. Creasey, T. Ikeda, and R. Tedrake, "Soft-bubble grippers for robust and perceptive manipulation," *Proc. IEEE/RSJ Int. Conf. Intelligent Robots and Systems (IROS)*, pp. 9917–9924, 2020.

[16] R. S. Dahiya, G. Metta, M. Valle, and G. Sandini, "Tactile sensing from humans to humanoids," *IEEE Trans. Robotics*, vol. 26, no. 1, pp. 1–20, 2010.

[17] B. Ward-Cherrier, N. Rojas, and N. F. Lepora, "Model-free precise in-hand manipulation with a 3D-printed tactile gripper," *IEEE Robotics and Automation Letters*, vol. 2, no. 4, pp. 2056–2063, 2017.

[18] M. Giorelli, F. Renda, G. Ferri, and C. Laschi, "A feed-forward neural network learning the inverse kinetics of a soft cable-driven manipulator moving in three-dimensional space," *Proc. IEEE/RSJ Int. Conf. Intelligent Robots and Systems (IROS)*, pp. 5033–5039, 2013.

[19] J. Hughes, U. Culha, F. Giardina, F. Guenther, A. Rosendo, and F. Iida, "Soft manipulators and grippers: A review," *Frontiers in Robotics and AI*, vol. 3, 2016.

[20] T. G. Thuruthel, B. Shih, C. Laschi, and M. T. Tolley, "Soft robot perception using embedded soft sensors and recurrent neural networks," *Science Robotics*, vol. 4, no. 26, 2019.

[21] Y. Nakamura and H. Hanafusa, "Inverse kinematic solutions with singularity robustness for robot manipulator control," *J. Dynamic Systems, Measurement, and Control*, vol. 108, no. 3, pp. 163–171, 1986.

[22] C. W. Wampler, "Manipulator inverse kinematic solutions based on vector formulations and damped least-squares methods," *IEEE Trans. Systems, Man, and Cybernetics*, vol. 16, no. 1, pp. 93–101, 1986.

[23] F. Chaumette and S. Hutchinson, "Visual servo control, Part I: Basic approaches," *IEEE Robotics and Automation Magazine*, vol. 13, no. 4, pp. 82–90, 2006.

[24] Y. B. Jia, F. Guo, and H. Lin, "Grasping deformable planar objects: Squeeze, stick/slip analysis, and energy-based optimalities," *Int. J. Robotics Research*, vol. 33, no. 6, pp. 866–897, 2014.

[25] R. D. Howe and M. R. Cutkosky, "Dynamic tactile sensing: Perception of fine surface features with stress rate sensing," *IEEE Trans. Robotics and Automation*, vol. 9, no. 2, pp. 140–151, 1993.